AIAA JOURNAL
Vol. 38, No. 10, October 2000

Dynamic Responses of Smart Composites Using a Coupled Thermo–Piezoelectric–Mechanical Model

Xu Zhou,* Aditi Chattopadhyay,† and Haozhong Gu‡
Arizona State University, Tempe, Arizona 85287-6106

A completely coupled thermo–piezoelectric–mechanical theory is developed to model the dynamic response of composite plates with surface-bonded piezoelectric actuators. A higher-order laminate theory is used to describe the displacement fields of both composite laminate and piezoelectric actuator layers to accurately model the transverse shear deformation, which is significant in moderately thick constructions. A higher-order temperature field is used to accurately describe the temperature distribution through the thickness of composite plates. A finite element model is developed to implement the theory. Thermal and piezoelectric loads are considered. The results obtained using this coupled theory are compared with those obtained using an uncoupled theory. Numerical results indicate that the thermo–piezoelectric–mechanical coupling has significant effect on the dynamic response of composite plates. Furthermore, coupling also affects the control authority of piezoelectric actuators.

Nomenclature

$\boldsymbol{B}$	= dielectric permittivity matrix
$\boldsymbol{B}_m, \boldsymbol{B}_n, \boldsymbol{B}_p, \boldsymbol{B}_u, \boldsymbol{B}_\theta, \boldsymbol{B}_\phi$	= operator matrices
b_{ij}	= dielectric permittivity, $i, j = 1, 2, 3$
$\boldsymbol{C}_{uu}, \boldsymbol{C}_{\theta u}, \boldsymbol{C}_{\theta\theta}, \boldsymbol{C}_{\theta\phi}$	= damping matrices
c_E	= heat capacity
c_{ijkl}	= elastic constants, $i, j, k, l = 1, 2, 3$
$\boldsymbol{D}$	= electric displacement vector
D_i	= components of electric displacement vector, $i = 1, 2, 3$
$\boldsymbol{d}$	= matrix of thermal–piezoelectric coupling constants
d_i	= thermal–piezoelectric coupling constants, $i = 1, 2, 3$
$\boldsymbol{E}$	= electric field vector
E_i	= components of the electric field vector, $i = 1, 2, 3$
e_{ijk}	= piezoelectric constants, $i, j, k = 1, 2, 3$
F	= free energy
$\boldsymbol{F}_u, \boldsymbol{F}_{u\theta}, \boldsymbol{F}_\theta, \boldsymbol{F}_{\theta\theta}, \boldsymbol{F}_\phi, \boldsymbol{F}_{\phi\theta}$	= force vectors
H	= plate thickness including piezoelectric layers
h	= plate thickness without piezoelectric layers
h_T	= thickness of single piezoelectric actuator
h_v	= thermal convection coefficient
$\boldsymbol{K}_{uu}, \boldsymbol{K}_{u\theta}, \boldsymbol{K}_{u\phi}, \boldsymbol{K}_{\theta\theta}, \boldsymbol{K}_{\phi u}, \boldsymbol{K}_{\phi\theta}, \boldsymbol{K}_{\phi\phi}$	= stiffness matrices
$\boldsymbol{k}$	= matrix of thermal–mechanical coupling constants
k_{ij}	= thermal–mechanical coupling constants, $i, j = 1, 2, 3$
$\boldsymbol{L}_m, \boldsymbol{L}_n, \boldsymbol{L}_p, \boldsymbol{L}_u, \boldsymbol{L}_\theta, \boldsymbol{L}_\phi$	= operator matrices
$\boldsymbol{M}$	= structural mass matrix
$\boldsymbol{N}_u, \boldsymbol{N}_\theta, \boldsymbol{N}_\phi$	= interpolation matrices for displacement, electrical, and temperature fields, respectively
$\boldsymbol{P}$	= matrix of piezoelectric constants
$\boldsymbol{Q}$	= elastic matrix
q_e	= charge density
q_t	= heat flux
S	= entropy density
T_0	= initial temperature
T_∞	= environment temperature
$\boldsymbol{t}$	= traction vector
t_i	= components of traction vector, $i = 1, 2, 3$
u_i	= displacement components, $i = 1, 2, 3$
$\boldsymbol{u}_u, \boldsymbol{u}_\theta, \boldsymbol{u}_\phi$	= field vectors of displacement, electric potential, and temperature, respectively
$\boldsymbol{u}_u^e, \boldsymbol{u}_\theta^e, \boldsymbol{u}_\phi^e$	= vectors of displacement, electric potential, and temperature, respectively, containing variables at the element nodes
α_T	= material constant, c_E / T_0
γ	= material damping constant
ε_{ij}	= components of strain tensor, $i, j = 1, 2, 3$
θ	= temperature rise from initial temperature T_0
κ_{ij}	= thermal conductivity, $i, j = 1, 2, 3$
$\pi_u, \pi_\theta, \pi_\phi$	= energy functionals for mechanical, electrical, and thermal fields, respectively
ρ	= mass density
σ_{ij}	= components of stress tensor, $i, j = 1, 2, 3$
ϕ	= electric potential

Superscripts

T	= transpose
$\cdot$	= first derivative with respect to time
$\cdot\cdot$	= second derivative with respect to time

Subscript

i	= first derivative with respect to coordinate x_i

Presented as Paper 99-1481 at the AIAA/ASME/ASCE/AHS/ASC 40th Structures, Structural Dynamics, and Materials Conference, St. Louis, MO, 12–15 April 1999; received 14 July 1999; revision received 8 January 2000; accepted for publication 21 February 2000.

*Graduate Research Assistant, Department of Mechanical and Aerospace Engineering.
†Professor, Department of Mechanical and Aerospace Engineering. Associate Fellow AIAA.
‡Postdoctoral Fellow, Department of Mechanical and Aerospace Engineering; currently Senior Engineer, P.O. Box 516, MC S064-2809, Design, Manufacturing and Producibility Simulation, The Boeing Company, St. Louis, MO 63166-0516. Member AIAA.

Introduction

THE development of smart composites offers great potential for advanced aerospace structural applications. Piezoelectric materials are employed as both actuators and sensors in the development of these structures by taking advantage of direct and converse piezoelectric effects. Active control using piezoelectric materials has been traditionally studied based on classical laminate theory (CLT), which ignores the transverse shear effects.[1,2] A refined

hybrid plate theory that combines the layerwise theory and an equivalent single-layer theory (ESL) along with linear piezoelectricity was developed[3] to model smart composite laminates. A higher-order theory that proved computationally more efficient and was capable of accurately capturing the transverse shear effects, for both thin and moderately thick laminates, was developed by Chattopadhyay and Gu.[4] In the analysis of smart structures, the coupling issues associated with thermal, piezoelectric, and mechanical fields play an important role. However, these issues are ignored in most applications. In most of the work, one-way coupling that only considers the effect of a known field on another field is used. The biway coupling between piezoelectric and mechanical fields was included in the hybrid plate theory developed by Mitchell and Reddy.[3] The thermal effect was studied by Mindlin[5] and Mukherjee and Sinha.[6] Following their work, the piezothermoelastic behavior of composite plates was addressed by Tauchert[7] using CLT and by Lee and Saravanos[8,9] using layerwise theory. In Refs. 5–9, a known thermal field was used to study the effect on mechanical and piezoelectric fields. The interactions between thermal and mechanical fields as well as thermal and piezoelectric fields were ignored. Recently, a coupled thermo–piezoelectric–mechanical (T–P–M) model was developed by Chattopadhyay et al.[10,11] to address the biway coupling issues associated with smart composites under thermal loads. In Ref. 10, a linear temperature field was used and only quasi-static responses were presented. This was followed by the development of a higher-order temperature field to accurately model the temperature distribution through laminates of moderately thick constructions.[11] The objective of the present paper is to further extend the coupled theory to model the dynamic response of smart composite plates subjected to thermal, piezoelectric, and mechanical loads. The higher-order displacement theory is used to describe the displacement field to account for properly the transverse shear stresses that are important in composites. The developed theory is, therefore, applicable to both thin and moderately thick constructions. The higher-order temperature field is used to accurately describe the temperature field while satisfying the thermal boundary conditions. The governing equations are derived by applying the principle of free energy and variational principles. The procedure is implemented using the finite element method. Numerical results are presented to investigate the differences between the coupled T–P–M model and the conventional one-way coupled model. The effect of these two models on control authority is also studied.

Mathematical Formulation

For the plate shown in Fig. 1, the total free energy of the structure can be written as

$$F(\varepsilon_{ij}, E_i, \theta) = \tfrac{1}{2}c_{ijkl}\varepsilon_{ij}\varepsilon_{kl} - e_{ijk}E_i\varepsilon_{jk} - \tfrac{1}{2}b_{ij}E_iE_j - k_{ij}\theta\varepsilon_{ij} - d_iE_i\theta - \tfrac{1}{2}a_T\theta^2 \tag{1}$$

where ε_{ij} are the components of the strain tensor, E_i are the components of the electric field vector, and θ is the temperature rise from the initial temperature T_0. The quantities c_{ijkl} and e_{ijk} represent elastic and piezoelectric constants, respectively, and b_{ij} is dielectric permittivity. The quantities k_{ij} and d_i refer to thermal–mechanical and thermal–piezoelectric coupling constants, respectively, and a_T is defined as c_E/T_0, where c_E is heat capacity. Only piezoelectric material with linear constitutive relations is considered in the present work. This implies constant material coefficients. Consequently, the constitutive relations are as follows:

$$\sigma_{ij} = \frac{\partial F}{\partial \varepsilon_{ij}} = c_{ijkl}\varepsilon_{kl} - e_{ijk}E_k - k_{ij}\theta \tag{2}$$

$$D_i = -\frac{\partial F}{\partial E_i} = e_{ijk}\varepsilon_{jk} + b_{ij}E_j + d_i\theta \tag{3}$$

$$S = -\frac{\partial F}{\partial \theta} = k_{ij}\varepsilon_{ij} + d_iE_i + a_T\theta \tag{4}$$

where σ_{ij} and D_i are the components of the stress tensor and the electric displacement vector, respectively, and S is entropy density. In vector form, they are

$$\boldsymbol{\sigma} = \boldsymbol{Q}\boldsymbol{\varepsilon} - \boldsymbol{P}\boldsymbol{E} - \boldsymbol{k}\theta \tag{5}$$

$$\boldsymbol{D} = \boldsymbol{P}^T\boldsymbol{\varepsilon} + \boldsymbol{B}\boldsymbol{E} + \boldsymbol{d}\theta \tag{6}$$

$$S = \boldsymbol{k}^T\boldsymbol{\varepsilon} + \boldsymbol{d}^T\boldsymbol{E} + \alpha_T\theta \tag{7}$$

where $\boldsymbol{\sigma}$ and $\boldsymbol{D}$ are the stress vector and the electric displacement vector, respectively, and $\boldsymbol{\varepsilon}$ and $\boldsymbol{E}$ are the strain vector and the electric field vector, respectively. The matrices $\boldsymbol{Q}$ and $\boldsymbol{B}$ denote elastic constants and dielectric permittivity, respectively. The matrices $\boldsymbol{P}$, $\boldsymbol{k}$, and $\boldsymbol{d}$ denote piezoelectric constants, thermal–mechanical coupling constants, and thermal–piezoelectric coupling constants, respectively. These material constants and matrices represent energy-delivering ability from one field to another field. Typically, larger value of piezoelectric constants are desirable from the standpoint of producing better actuation capability and sensitivity, whereas smaller values of thermal–mechanical coupling and thermal–piezoelectric coupling constants are desirable for better thermal stability.

Based on linear piezoelectricity, E_i is derivable from a scalar potential function ϕ as follows:

$$E_i = -\phi_{,i}, \qquad i = 1, 2, 3 \tag{8}$$

The governing equations are now derived using variational principles as follows:

$$\delta\pi_u = -\int_0^{t_0}\int_V (\rho\ddot{u}_i\delta u_i + \gamma\dot{u}_i\delta u_i + \sigma_{ij}\delta\varepsilon_{ij})\,\mathrm{d}V\,\mathrm{d}t + \int_0^{t_0}\int_S t_i\delta u_i\,\mathrm{d}S\,\mathrm{d}t = 0 \tag{9}$$

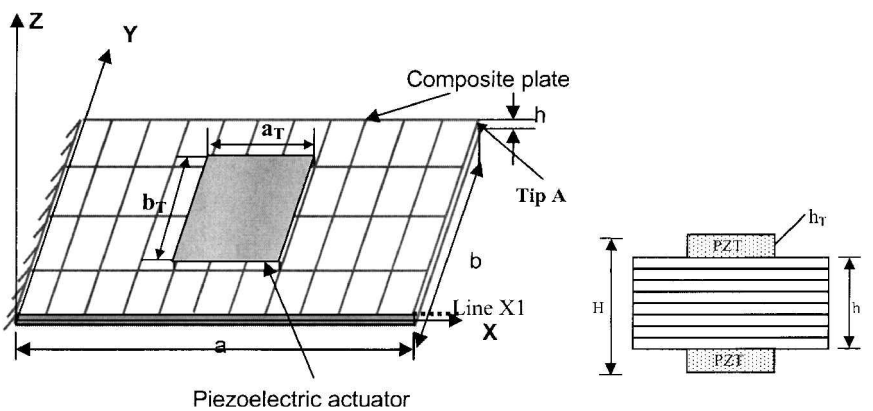

Fig. 1 Geometry and finite element model of composite laminate.

$$\delta\pi_\phi = -\int_0^{t_0}\int_V D_i\,\delta\phi_{,i}\,\mathrm{d}V\,\mathrm{d}t + \int_0^{t_0}\int_S q_e\,\delta\phi\,\mathrm{d}S\,\mathrm{d}t = 0 \tag{10}$$

$$\delta\pi_\theta = \int_0^{t_0}\int_V (\kappa_{ij}\theta_{,i}\delta\theta_{,j} + \dot{S}T_0\delta\theta)\,\mathrm{d}V\,\mathrm{d}t + \int_0^{t_0}\int_S q_t\,\delta\theta\,\mathrm{d}S\,\mathrm{d}t = 0 \tag{11}$$

where π_u, π_ϕ, and π_θ denote the energy functionals of mechanical, electrical, and thermal fields, respectively. The qualities ρ, γ, and κ_{ij} denote mass density, material damping constant, and material thermal conductivity, respectively. $\dot{S}$ denotes the time derivative of S, t_i represents the components of the traction vector, and q_e represents the charge density. The quantity q_t represents a specific heat flux or a convective heat flux defined as follows:

$$q_t = h_v(\theta + T_0 - T_\infty) \tag{12}$$

In Eq. (12), h_v is thermal convection coefficient, and T_0 and T_∞ are the initial temperature and environment temperature, respectively.

The displacement field is modeled using the higher-order theory that incorporates the transverse shear effects. The form is dictated by the satisfaction of the conditions that the transverse shear stresses vanish on plate surfaces and are nonzero elsewhere. The higher-order displacement field is written as follows[4,10]:

$$u_1(x, y, z, t) = u_0(x, y, t) - z\frac{\partial w_0(x, y, t)}{\partial x} + g(z)\psi_x(x, y, t) \tag{13}$$

$$u_2(x, y, z, t) = v_0(x, y, t) - z\frac{\partial w_0(x, y, t)}{\partial y} + g(z)\psi_y(x, y, t) \tag{14}$$

$$u_3(x, y, z, t) = w_0(x, y, t) \tag{15}$$

with

$$g(z) = z - (4/3H^2)z^3 \tag{16}$$

In Eqs. (13–15), u_0, v_0, and w_0 are the displacements of a point in the midplane of the laminate, ψ_x and ψ_y are the rotations of a transverse normal at $z = 0$ about the y and the $-x$ axes, respectively, and H indicates the total thickness of the plate including the piezoelectric layers (Fig. 1).

The potential function ϕ is assumed to be linear along z axis in each piezoelectric layer:

$$\phi(x, y, z, t) = \phi_0(x, y, t) + z\phi_1(x, y, t) \tag{17}$$

where the functions $\phi_0(x, y, t)$ and $\phi_1(x, y, t)$ define the in-plane electric potential variations.

Based on the higher-order temperature theory,[11] the temperature field θ is assumed as a cubic function of the thickness of the plate z:

$$\theta(x, y, z, t) = f(z) + p_1(z)\theta_0(x, y, t) + p_2(z)\theta_1(x, y, t) \tag{18}$$

where the functions $\theta_0(x, y, t)$ and $\theta_1(x, y, t)$ define the in-plane temperature variations. The cubic functions $f(z)$, $p_1(z)$, and $p_2(z)$ denote the temperature variations through the plate thickness. Detailed definitions of $f(z)$, $p_1(z)$, and $p_2(z)$ are presented in Appendix A. Compared to the linear temperature field assumption, generally used in plate problems to define the temperature variation through the plate thickness, the cubic functions in Eq. (18) can satisfy thermal boundary conditions on the plate surfaces and model the temperature field through the plate thickness accurately.

When we use Eqs. (13–15), the strain vector $\boldsymbol{\varepsilon}$ and the displacement vector $\boldsymbol{u}$ can be written as follows:

$$\boldsymbol{\varepsilon} = \begin{Bmatrix}\varepsilon_1\\ \varepsilon_2\\ \varepsilon_4\\ \varepsilon_5\\ \varepsilon_6\end{Bmatrix} = \begin{Bmatrix}\dfrac{\partial u_1}{\partial x}\\ \dfrac{\partial u_2}{\partial y}\\ \dfrac{\partial u_2}{\partial z} + \dfrac{\partial u_3}{\partial y}\\ \dfrac{\partial u_1}{\partial z} + \dfrac{\partial u_3}{\partial x}\\ \dfrac{\partial u_1}{\partial y} + \dfrac{\partial u_2}{\partial x}\end{Bmatrix}$$

$$= \begin{bmatrix}\dfrac{\partial}{\partial x} & 0 & -z\dfrac{\partial^2}{\partial x^2} & g(z)\dfrac{\partial}{\partial x} & 0\\ 0 & \dfrac{\partial}{\partial y} & -z\dfrac{\partial^2}{\partial y^2} & 0 & g(z)\dfrac{\partial}{\partial y}\\ 0 & 0 & 0 & 0 & \dfrac{\mathrm{d}}{\mathrm{d}z}g(z)\\ 0 & 0 & 0 & \dfrac{\mathrm{d}}{\mathrm{d}z}g(z) & 0\\ \dfrac{\partial}{\partial y} & \dfrac{\partial}{\partial x} & -2z\dfrac{\partial^2}{\partial x\,\partial y} & g(z)\dfrac{\partial}{\partial y} & g(z)\dfrac{\partial}{\partial x}\end{bmatrix}\begin{Bmatrix}u_0\\ v_0\\ w_0\\ \psi_x\\ \psi_y\end{Bmatrix}$$

$$= \boldsymbol{L}_u\boldsymbol{u}_u \tag{19}$$

$$\boldsymbol{u} = \begin{Bmatrix}u_1\\ u_2\\ u_3\end{Bmatrix} = \begin{bmatrix}1 & 0 & -z\dfrac{\partial}{\partial x} & g(z) & 0\\ 0 & 1 & -z\dfrac{\partial}{\partial y} & 0 & g(z)\\ 0 & 0 & 1 & 0 & 0\end{bmatrix}\begin{Bmatrix}u_0\\ v_0\\ w_0\\ \psi_x\\ \psi_y\end{Bmatrix} = \boldsymbol{L}_m\boldsymbol{u}_u \tag{20}$$

with

$$\boldsymbol{u}_u = \boldsymbol{N}_u(x, y)\boldsymbol{u}_u^e \tag{21}$$

where $\boldsymbol{u}_u$ is a displacement field vector, $\boldsymbol{u}_u^e$ is a vector containing the displacement variables at element nodes, and $\boldsymbol{N}_u(x, y)$ is an interpolation matrix. The strain and the displacement vectors now take the following form:

$$\boldsymbol{\varepsilon} = \boldsymbol{B}_u\boldsymbol{u}_u^e \tag{22}$$

$$\boldsymbol{u} = \boldsymbol{B}_m\boldsymbol{u}_u^e \tag{23}$$

where

$$\boldsymbol{B}_u = \boldsymbol{L}_u\boldsymbol{N}_u(x, y) \tag{24}$$

$$\boldsymbol{B}_m = \boldsymbol{L}_m\boldsymbol{N}_u(x, y) \tag{25}$$

The expressions for the electric field vector $\boldsymbol{E}$ and the potential function ϕ can be written as follows:

$$\boldsymbol{E} = -\begin{Bmatrix}\dfrac{\partial\phi}{\partial x}\\ \dfrac{\partial\phi}{\partial y}\\ \dfrac{\partial\phi}{\partial z}\end{Bmatrix} = -\begin{bmatrix}\dfrac{\partial}{\partial x} & z\dfrac{\partial}{\partial x}\\ \dfrac{\partial}{\partial y} & z\dfrac{\partial}{\partial y}\\ 0 & 1\end{bmatrix}\begin{Bmatrix}\phi_0\\ \phi_1\end{Bmatrix} = \boldsymbol{L}_\phi\boldsymbol{u}_\phi \tag{26}$$

$$\phi = [1 \quad z]\begin{Bmatrix}\phi_0\\ \phi_1\end{Bmatrix} = \boldsymbol{L}_n\boldsymbol{u}_\phi \tag{27}$$

with

$$\boldsymbol{u}_\phi = \boldsymbol{N}_\phi(x, y)\boldsymbol{u}_\phi^e \tag{28}$$

where $\boldsymbol{u}_\phi$ is an electric potential vector, $\boldsymbol{u}_\phi^e$ represents the potential variables at element nodes, and $\boldsymbol{N}_\phi(x, y)$ is an interpolation matrix. The electric field vector and the potential function now take the following form:

$$\boldsymbol{E} = \boldsymbol{B}_\phi\boldsymbol{u}_\phi^e \tag{29}$$

$$\phi = \boldsymbol{B}_n\boldsymbol{u}_\phi^e \tag{30}$$

where

$$\boldsymbol{B}_\phi = \boldsymbol{L}_\phi \boldsymbol{N}_\phi(x, y) \tag{31}$$

$$\boldsymbol{B}_n = \boldsymbol{L}_n \boldsymbol{N}_\phi(x, y) \tag{32}$$

The expressions for the temperature field θ and its gradient $\theta_{,i}$, $i = 1, 2, 3$, can be written as follows:

$$\theta = f(z) + [p_1(z) \quad p_2(z)] \begin{Bmatrix} \theta_0 \\ \theta_1 \end{Bmatrix} = f(z) + \boldsymbol{L}_\theta \boldsymbol{u}_\theta \tag{33}$$

$$\theta_{,i} = \begin{Bmatrix} \dfrac{\partial \theta}{\partial x} \\ \dfrac{\partial \theta}{\partial y} \\ \dfrac{\partial \theta}{\partial z} \end{Bmatrix} = \begin{Bmatrix} 0 \\ 0 \\ \dfrac{\mathrm{d}}{\mathrm{d}z} f(z) \end{Bmatrix} + \begin{bmatrix} p_1(z)\dfrac{\partial}{\partial x} & p_2(z)\dfrac{\partial}{\partial x} \\ p_1(z)\dfrac{\partial}{\partial y} & p_2(z)\dfrac{\partial}{\partial y} \\ \dfrac{\mathrm{d}}{\mathrm{d}z} p_1(z) & \dfrac{\mathrm{d}}{\mathrm{d}z} p_2(z) \end{bmatrix}$$

$$\begin{Bmatrix} \theta_0 \\ \theta_1 \end{Bmatrix} = \begin{Bmatrix} 0 \\ 0 \\ \dfrac{\mathrm{d}}{\mathrm{d}z} f(z) \end{Bmatrix} + \boldsymbol{L}_p \boldsymbol{u}_\theta \tag{34}$$

with

$$\boldsymbol{u}_\theta = \boldsymbol{N}_\theta(x, y) \boldsymbol{u}_\theta^e \tag{35}$$

where $\boldsymbol{u}_\theta$ is a temperature field vector, $\boldsymbol{u}_\theta^e$ is a vector containing the nodal values, and $\boldsymbol{N}_\theta(x, y)$ is an interpolation matrix. The temperature field and its gradient now take the following form:

$$\theta = f(z) + \boldsymbol{B}_\theta \boldsymbol{u}_\theta^e \tag{36}$$

$$\theta_{,i} = \begin{bmatrix} 0 & 0 & \dfrac{\mathrm{d}}{\mathrm{d}z} f(z) \end{bmatrix}^T + \boldsymbol{B}_p \boldsymbol{u}_\theta^e \tag{37}$$

where

$$\boldsymbol{B}_\theta = \boldsymbol{L}_\theta \boldsymbol{N}_\theta(x, y) \tag{38}$$

$$\boldsymbol{B}_p = \boldsymbol{L}_p \boldsymbol{N}_\theta(x, y) \tag{39}$$

The use of Eqs. (2–4), (22), (23), (29), (30), (36), and (37) in Eqs. (9–11) and integration with respect to volume V yields the following:

$$\delta\pi_u = \delta \boldsymbol{u}_u^{eT} \int_0^{t_0} \Big(-\boldsymbol{M}\ddot{\boldsymbol{u}}_u^e - \boldsymbol{C}_{uu}\dot{\boldsymbol{u}}_u^e - \boldsymbol{K}_{uu}\boldsymbol{u}_u^e - \boldsymbol{K}_{u\phi}\boldsymbol{u}_\phi^e - \boldsymbol{K}_{u\theta}\boldsymbol{u}_\theta^e + \boldsymbol{F}_{u\theta} + \boldsymbol{F}_u \Big)\, \mathrm{d}t \tag{40}$$

$$\delta\pi_\phi = \delta \boldsymbol{u}_\phi^{eT} \int_0^{t_0} \Big(-\boldsymbol{K}_{\phi u}\boldsymbol{u}_u^e - \boldsymbol{K}_{\phi\phi}\boldsymbol{u}_\phi^e - \boldsymbol{K}_{\phi\theta}\boldsymbol{u}_\theta^e + \boldsymbol{F}_{\phi\theta} + \boldsymbol{F}_\phi \Big)\, \mathrm{d}t \tag{41}$$

$$\delta\pi_\theta = \delta \boldsymbol{u}_\theta^{eT} \int_0^{t_0} \Big(-\boldsymbol{C}_{\theta u}\dot{\boldsymbol{u}}_u^e - \boldsymbol{C}_{\theta\phi}\dot{\boldsymbol{u}}_\phi^e - \boldsymbol{C}_{\theta\theta}\dot{\boldsymbol{u}}_u^e - \boldsymbol{K}_{\theta\theta}\boldsymbol{u}_u^e + \boldsymbol{F}_{\theta\theta} + \boldsymbol{F}_\theta \Big)\, \mathrm{d}t \tag{42}$$

When we substitute Eqs. (40–42) into Eqs. (9–11), the finite element governing equations of the completely coupled (T–P–M) theory, based on the higher-order displacement field and the higher-order temperature field, are obtained and are written in matrix form as follows:

$$\begin{bmatrix} \boldsymbol{M} & 0 & 0 \\ 0 & 0 & 0 \\ 0 & 0 & 0 \end{bmatrix} \begin{Bmatrix} \ddot{\boldsymbol{u}}_u^e \\ \ddot{\boldsymbol{u}}_\phi^e \\ \ddot{\boldsymbol{u}}_\theta^e \end{Bmatrix} + \begin{bmatrix} \boldsymbol{C}_{uu} & 0 & 0 \\ 0 & 0 & 0 \\ \boldsymbol{C}_{\theta u} & \boldsymbol{C}_{\theta\phi} & \boldsymbol{C}_{\theta\theta} \end{bmatrix} \begin{Bmatrix} \dot{\boldsymbol{u}}_u^e \\ \dot{\boldsymbol{u}}_\phi^e \\ \dot{\boldsymbol{u}}_\theta^e \end{Bmatrix} + \begin{bmatrix} \boldsymbol{K}_{uu} & \boldsymbol{K}_{u\phi} & \boldsymbol{K}_{u\theta} \\ \boldsymbol{K}_{\phi u} & \boldsymbol{K}_{\phi\phi} & \boldsymbol{K}_{\phi\theta} \\ 0 & 0 & \boldsymbol{K}_{\theta\theta} \end{bmatrix} \begin{Bmatrix} \boldsymbol{u}_u^e \\ \boldsymbol{u}_\phi^e \\ \boldsymbol{u}_\theta^e \end{Bmatrix} = \begin{Bmatrix} \boldsymbol{F}_u + \boldsymbol{F}_{u\theta} \\ \boldsymbol{F}_\phi + \boldsymbol{F}_{\phi\theta} \\ \boldsymbol{F}_\theta + \boldsymbol{F}_{\theta\theta} \end{Bmatrix} \tag{43}$$

where $\boldsymbol{M}$ is the structural mass matrix. The matrices $\boldsymbol{C}_{\theta u}$ and $\boldsymbol{C}_{\theta\phi}$ are damping matrices due to thermal–mechanical coupling (piezocaloric) and thermal–electrical coupling (electrocaloric), respectively. The existence of these matrices in the governing equations leads to dissipation of thermal energy generated from mechanical and piezoelectric fields. The matrices $\boldsymbol{C}_{uu}$ and $\boldsymbol{C}_{\theta\theta}$ are structural damping matrix and damping matrix representing thermal energy diffusion, respectively. The presence of all of these damping terms influences the dynamic response decay. The matrices $\boldsymbol{K}_{u\phi}$ and $\boldsymbol{K}_{\phi u}$ are stiffness matrices due to piezoelectric–mechanical coupling (converse piezoelectric and piezoelectric). Their presence allows piezoelectric materials to produce mechanical actuation forces under input voltages or electrical signals under mechanical deformations. The matrices $\boldsymbol{K}_{u\theta}$ and $\boldsymbol{K}_{\phi\theta}$ are stiffness matrices due to thermal–mechanical coupling (pyrostriction) and thermal–electrical coupling (pyroelectric), respectively. Note that the thermal energy generated from mechanical and piezoelectric fields dissipates as damping ($\boldsymbol{C}_{\theta u}$ and $\boldsymbol{C}_{\theta\phi}$), whereas the mechanical and electrical energies generated from thermal field are retained as system stiffness. The matrices $\boldsymbol{K}_{uu}$, $\boldsymbol{K}_{\phi\phi}$, and $\boldsymbol{K}_{\theta\theta}$ are stiffness matrices resulting from mechanical, electrical, and thermal fields, respectively. The stiffness coupling effects can influence the equilibrium position if a steady state exists. The vectors $\boldsymbol{F}_u$, $\boldsymbol{F}_\phi$, and $\boldsymbol{F}_\theta$ are force vectors due to mechanical, electrical, and thermal fields, respectively, and the vectors $\boldsymbol{F}_{u\theta}$, $\boldsymbol{F}_{\phi\theta}$, and $\boldsymbol{F}_{\theta\theta}$ result from the higher-order temperature field. The exact definitions of these matrices [Eq. (43)] are presented in Appendix B.

Results and Discussion

In most reported work, only the standard ("uncoupled") model, with one-way coupling between mechanical, electrical, and thermal fields, is considered. The uncoupled model neglects coupling effects on both equilibrium position (steady state) and energy dissipation due to damping. For example, in the analysis of piezoelectric actuators under thermal loads, using the uncoupled model, only converse piezoelectric and pyrostriction effects are considered. Piezoelectric, pyroelectric, piezocaloric, and electrocaloric effects are neglected. To illustrate the importance of including these effects, comparisons of the completely coupled T–P–M model are made with the uncoupled model for piezoelectric actuators.

In the numerical analysis, a rectangular fiber-reinforced laminated composite plate with surface-bonded piezoelectric actuators, at the center of top and bottom surfaces of the plate, is considered (Fig. 1). The plate is fixed at one end, and the remaining edges are free. The plate dimensions are such that length $a = 0.3048$ m and width $b = 0.1524$ m. Results are presented for two different plate thicknesses, $h = 0.003048$ m ($a/h = 100$, thin plate) and $h = 0.01524$ m ($a/h = 20$, thick plate). The stacking sequence is $[0/90/0/90\ \mathrm{deg}]_s$. The piezoelectric actuator is of length $a_T = 0.4a$, width $b_T = 0.5b$, and thickness $h_T = 0.25h$. The material constants for the composite and the piezoelectric material are listed in Table 1. The tip position of the structure denotes point A in Fig. 1. A four-node plate element is used to discretize the plate structure (Fig. 1). To fully understand the coupling issues, it is necessary to evaluate the impact of the various coupling matrices [Eq. (43)]. Therefore, in-depth numerical studies are conducted to understand their physical significance.

Damping due to Piezocaloric and Electrocaloric Effects

The analysis of energy dissipation caused by the presence of additional damping [$C_{\theta u}$ and $C_{\theta\phi}$, Eq. (43)], due to piezocaloric and electrocaloric coupling effects in the T–P–M model, is performed by solving the eigenvalue problem of Eq. (43). The damping matrices $C_{\theta u}$ and $C_{\theta\phi}$, although directly related to the thermal equilibrium equation, can be considered equivalent to structural damping. This is because the coupling relationship between thermal and mechanical fields allows this effect to be captured in the different eigenmodes of the mechanical response. The variation of the equivalent structural damping with reference temperature T_0 is presented for the thin plate in Fig. 2. It can be observed that the equivalent structural damping is small (10^{-7}–10^{-6}) compared to general structural damping (10^{-3}–10^{-2}). Also, the damping is linearly proportional to the reference temperature T_0, which is in agreement with the variations of $C_{\theta u}$

Table 1 Material properties of piezoelectric and graphite/epoxy composite

Parameter	Piezoelectric	Graphite/epoxy
Elastic moduli, GPa		
E_{11}	63	144.23
E_{22}	63	9.65
E_{33}	63	9.65
Shear moduli, GPa		
G_{23}	24.6	3.45
G_{13}	24.6	4.14
G_{12}	24.6	4.14
Poisson's ratio		
ν	0.28	0.3
Coefficients of thermal expansion, μm/m · °C		
α_{11}	0.9	1.1
α_{22}	0.9	25.2
Density, kg/m^3		
ρ	7600	1389.23
Piezoelectric charge constant, pm/V		
$e_{31} = e_{32}$	250	——
Electric permittivity, nF/m		
$b_{11} = b_{22}$	15.3	——
b_{33}	15.0	——
Pyroelectric constant, μC/m^2 · °C		
d_3	20	——
Thermal conductivity, W/m · °C		
κ_{11}	2.1	4.48
κ_{22}	2.1	3.21
Heat capacity, J/kg°C		
c_E	420	1409
Thermal convection coefficient, W/m^2 · °C		
h_v	20.0	20.0
Curie temperature, °C		
T_c	365	——

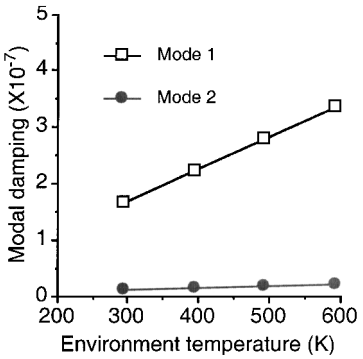

Fig. 2 Equivalent structural damping: T–P–M model, $a/h = 100$.

and $C_{\theta\phi}$ with T_0 [Eqs. (B10) and (B11)]. Therefore, the damping effects due to piezocaloric and electrocaloric couplings in the T–P–M model should be evaluated based on the reference temperature, thermal–mechanical, and thermal–piezoelectric coupling constants of the piezoelectric material used.

Piezoelectric Actuation Effects and Parametric Studies

A comparison of piezoelectric actuation effects using the T–P–M model and the uncoupled model is performed. The same plate structure without thermal and mechanical loading is considered. Both top and bottom actuators are subjected to a step voltage load of the same magnitude but opposite directions, making out-of-plane deformation dominant. In this case, the T–P–M model for actuators represents biway mechanical–piezoelectric coupling (piezoelectric and converse piezoelectric effects), whereas the uncoupled model represents only one-way mechanical–piezoelectric coupling (converse piezoelectric effect). The steady-state tip deflections for the thin plate ($a/h = 100$), under varying piezoelectric actuation, are presented in Fig. 3. It can be seen that the equilibrium deflection of tip position is directly proportional to the magnitude of the external voltage. The T–P–M model predicts a smaller deformation compared to the uncoupled model. This is because more transformation of mechanical energy into thermal and electric energies due to the biway coupling effect is considered in the T–P–M model. To illustrate the differences clearly, the ratio of the difference between the deflections obtained using the two models to the deflection obtained using the uncoupled model, defined as NRD (normalized relative difference), is also plotted in Fig. 3 sharing the same axis with tip deflection. The value of NRD is about 21% with the uncoupled model overpredicting the displacement. The magnitude of NRD remains almost insensitive to input voltage because the deflections vary proportionately with the magnitude of the external voltages in both models. The steady-state deflections along plate length (line X1, Fig. 1) due to a piezoelectric actuation of 50 V are presented in Fig. 4. The dynamic tip responses due to a step piezoelectric actuation of 50 V are presented in Fig. 5. From Figs. 4 and 5, a smaller steady-state (static) deflection and a smaller amplitude of vibration are observed in the T–P–M model due to the presence of coupling.

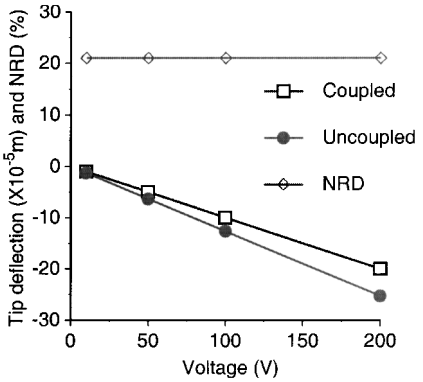

Fig. 3 Variation in tip deflections and NRD with piezoelectric actuation: $a/h = 100$.

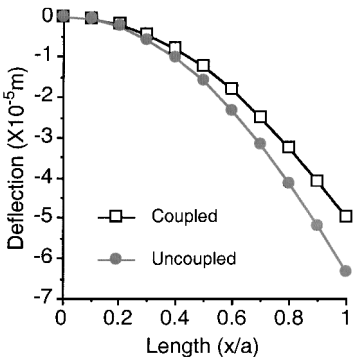

Fig. 4 Deflections along plate length with piezoelectric actuation: 50 V, $a/h = 100$.

A similar investigation is performed with the thick plate ($a/h = 20$). Figure 6 presents the steady-state deflections along plate length (line X1, Fig. 1) due to the piezoelectric actuation of 50 V, and Fig. 7 presents the corresponding comparison of the dynamic tip responses. Much smaller deflections and vibration amplitudes are observed with both the T–P–M model and the uncoupled model compared to the thin plate case due to larger structural stiffness. However, the NRD in tip deflection, between the two models, is still significant (about 21%). Note that in this case a thicker piezoelectric actuator is used because the actuator thickness $h_T = 0.25h$. This implies that the thickness ratio of actuator to plate, in both the thin and the thick plate cases, is maintained the same, which causes the NRD to remain unchanged between the two cases.

Figure 8 presents results of the parametric studies for the thin plate. Figure 8a illustrates the variation of NRD in equilibrium deflection of tip position with changes in plate length-to-width ratio a/b with a step piezoelectric actuation of 50 V. A small length-to-width ratio implies a greater effect of mechanical boundary constraints because the plate is fixed along the width. The deviation is expected to increase with an increase in the value of a/b. However, the volume ratio of actuator to host plate is a parameter that has more influence on the mechanical–piezoelectric coupling

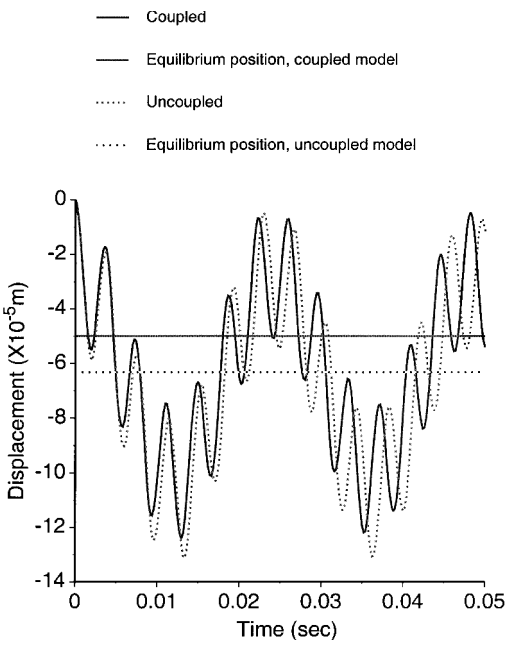

Fig. 5 Dynamic tip responses with step piezoelectric actuation: 50 V, $a/h = 100$.

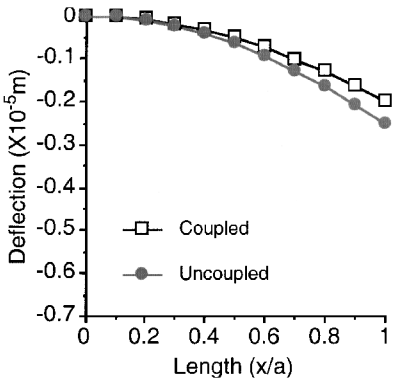

Fig. 6 Deflections along plate length with piezoelectric actuation: 50 V, $a/h = 20$.

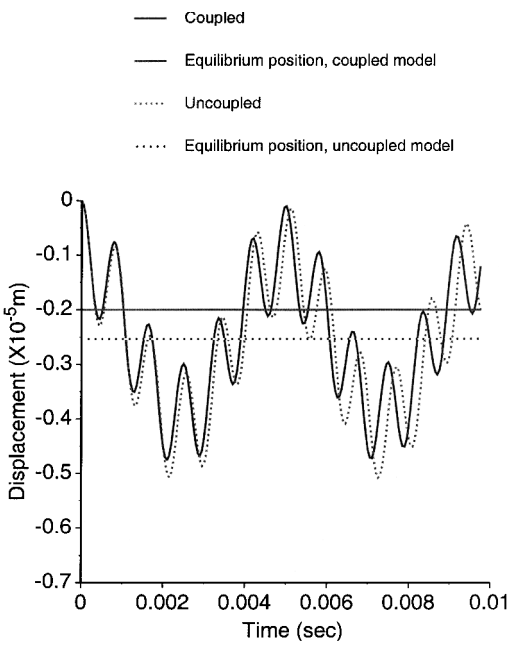

Fig. 7 Dynamic tip responses with step piezoelectric actuation: 50 V $a/h = 20$.

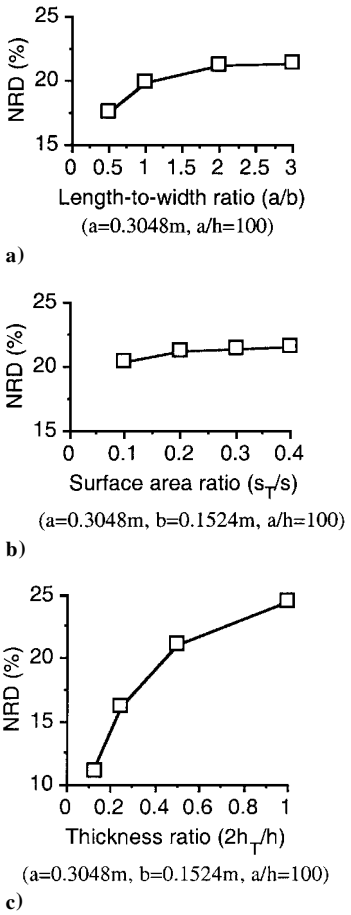

Fig. 8 Variation in NRD with structure geometry with piezoelectic actuation: 50 V.

effect for a given structure. In this case, because the actuator dimensions are proportional to plate dimensions, the volume ratio does not vary with a/b. Therefore, the deviation between the two models increases only slightly with an increase in the length-to-width ratio. Figure 8b illustrates the variation of NRD in the equilibrium deflection of tip position with changes in the surface-area ratio of bonded actuator to host plate s_T/s while the thicknesses are held fixed. The variation in surface-area ratio is realized by changing the actuator length. The plate dimensions and the actuator width remain unchanged, and the actuator center coincides with the plate center. It is observed that the NRD, between the two models, shows very little variation with surface-area ratio. This is because in this case, the actuator strain depends on the stiffness ratio of actuator to plate. With increased actuator area, the changes in the average strain within the actuator that lead to the coupling effects are insignificant. Therefore, only slight variation is observed with changes in surface-area ratio. Figure 8c illustrates the variation of NRD in equilibrium deflection of tip position with changes in thickness ratio of actuator to plate $2h_T/h$ while length and width of the plate and the actuators are held fixed. An increase in $2h_T/h$ implies that there is more electric energy generated from the mechanical field that can be stored in piezoelectric actuators. Therefore, the coupling effects are stronger and the NRD increases rapidly.

Thermal Actuation Effects and Parametric Studies

Numerical analysis with only thermal excitations is performed to investigate thermal coupling effects. The same plate configuration is used. A uniform step heat flux is applied on the top surface of the plate, and the structure is insulated at the bottom. All four sides are maintained at room temperature (20°C). Thermal steady state is achieved when there is an equilibrium between the inflow of surface heat flux and heat outflow through the four sides of the plate. Note that although there is no external voltage, all coupling effects between thermal, piezoelectric, and mechanical fields are still present

in the T–P–M model. Only the coupling effects of pyrostriction and converse piezoelectric effect are present in the uncoupled model. Results for the thin plate ($a/h = 100$) are presented in Figs. 9–11. The steady-state tip deflections and the NRD with different specified heat fluxes on the top surface are presented in Fig. 9. The steady-state deflections along plate length (line X1, Fig. 1) with a heat flux $q_t = 3000$ W/m^2 applied on the top surface are presented in Fig. 10. The coupling effects in the T–P–M model result in a smaller steady-state deflection compared to the uncoupled model. A deviation of about 5% is observed in the value of the tip deflection, which is much smaller compared to the case with only piezoelectric actuation (21%, Fig. 3). This is because pyrostriction, the principal source of thermally induced deformation, is considered in both the T–P–M and the uncoupled models. The difference in equilibrium position between the two models is due to the piezoelectric effect of a thermally induced electrical field, which is neglected in the uncoupled model. Therefore, the NRD in this case is smaller compared to the piezoelectric actuation case, where the deviation is directly driven by the piezoelectric effect of actuation. Figure 11 presents the time history of the tip displacement until steady state is reached. A smaller steady-state tip deflection is observed with the T–P–M model. Because the damping effect due to $\boldsymbol{C}_{\theta u}$ and $\boldsymbol{C}_{\theta\phi}$ [Eq. (43)], considered only in the T–P–M model, is small, no significant difference between the two models is observed in the dynamic response decay. In both cases, steady state is achieved in about 3 s. Results for the thick plate ($a/h = 20$) are presented in Figs. 12 and 13. Figure 12 presents the steady-state deflections along the plate length (line X1, Fig. 1) with a heat flux $q_t = 3000$ W/m^2 applied on the top surface. Once again, the coupling effect introduces an additional 5% reduction in tip deflection (NRD) compared to the uncoupled case. The deflections are comparable to those obtained in the case of the thin plate under the same heat flux. This is because unlike the case of deformation due to a mechanical force, thermally induced plate deformation primarily depends on the average temperature slope through the thickness, which is almost the same for the thin and the thick plates in this example. Figure 13 presents the time history of tip displacement until steady state is achieved. Vibrations reduce in less than 1 s due to higher frequencies of the thick plate. However, the temperature distribution and the induced deformation require a much longer time (more than 50 s) to reach steady state. A significant reduction (5% NRD) in steady-state deflection is also observed when coupling effects are included. These results (Figs. 9–13) clearly demonstrate the importance of including the T–P–M coupling effects to model the behavior of composite structures subjected to thermal loads.

The difference between the two models in the presence of thermal actuation is investigated by varying the plate length-to-width ratio (a/b). The plate dimensions are such that $a = 0.3048$ m and $h = 0.003048$ m ($a/h = 100$). Once again, the volume ratio of actuator to plate does not vary with variation in a/b. Figure 14 illustrates that the steady-state deflections show a rapid increase initially ($0.5 \leq a/b \leq 1.5$). With a further increase in a/b, the deflections show very little variation. The trend is similar in both models. This can also be explained by the influence of mechanical boundary constraints decreasing with an increase in the length-to-width ratio.

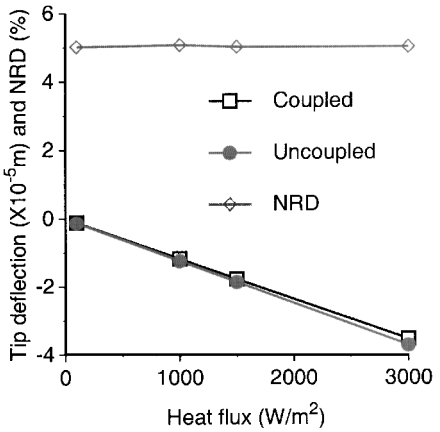

Fig. 9 Variation in tip deflections and NRD with surface heat flux: $a/h = 100$.

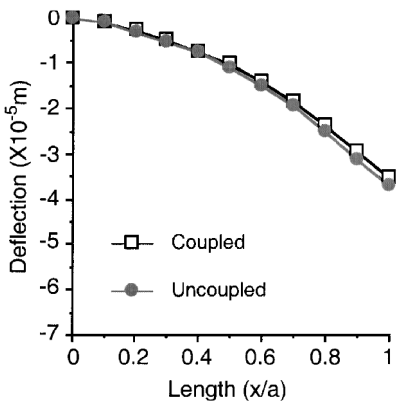

Fig. 10 Deflections along plate length with surface heat flux: q_t = 3000 W/m^2, $a/h = 100$.

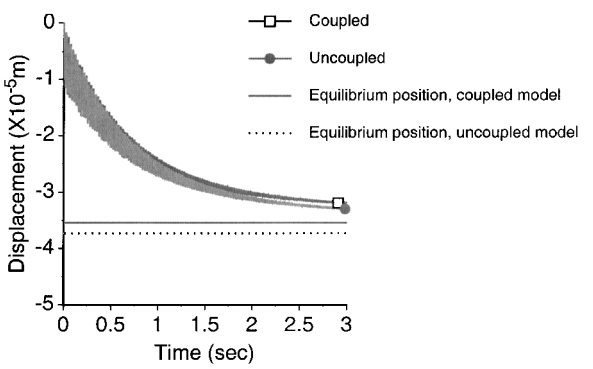

Fig. 11 Dynamic tip responses with step surface heat flux: $q_t = 3000$ W/m^2, $a/h = 100$.

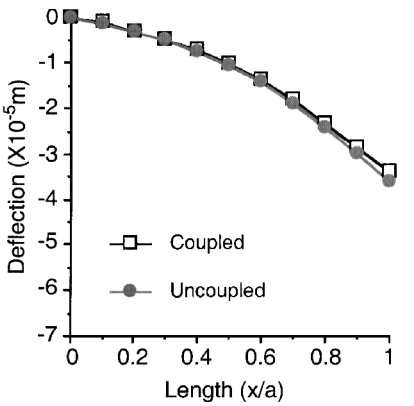

Fig. 12 Deflections along plate length with surface heat flux: q_t = 3000 W/m^2, $a/h = 20$.

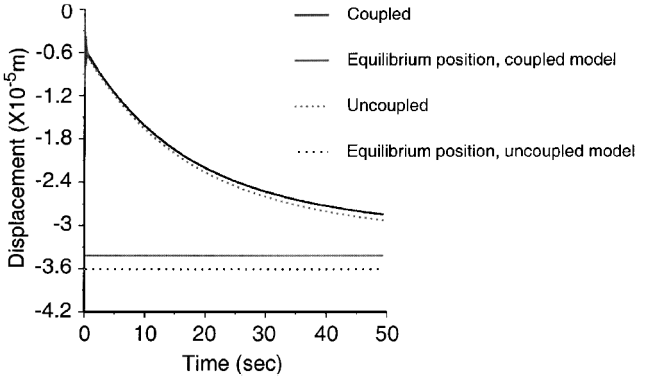

Fig. 13 Dynamic tip responses with step surface heat flux: q_t = 3000 W/m^2, $a/h = 20$.

Therefore, the ratio a/b has a greater effect on steady-state deflections compared to the ratio a/h. It is also observed that the deviation between the two models varies only slightly with an increase in a/b. This is because even in the pure thermal loading case, the deviation between the two models is caused by a piezoelectric–mechanical coupling effect due to a thermally induced electrical field in the actuators, which is represented by pyroelectric and piezoelectric effects of actuators. Therefore, the volume ratio of actuator to host plate is a governing factor in assessing thermal coupling effects. Thermal–electrical coupling effect cannot be neglected, particularly when the volume ratio of actuator to host plate is large.

Dynamic Control

An important issue to be analyzed is the impact of modeling on control authority. To investigate this, the thin plate ($a/h = 100$) with self-sensing piezoelectric actuators, surface bonded to the top and bottom surfaces, is considered. Rate feedback control is employed. An initial velocity disturbance is used to excite the first bending mode, which can be controlled by the actuators located at the center of the plate. Figures 15 and 16 present the time histories of tip displacement over the first four cycles with a gain value of 50 and 100, respectively. The results from both the T–P–M model and the uncoupled model are presented with and without control. The amplitude of displacement is reduced with control in both cases. Initially, very little difference between the two models is observed in the displacement without control. With the application of control, during the first cycle, smaller vibration amplitudes are predicted by the uncoupled model compared to the T–P–M model (Figs. 15 and 16). In other words, the uncoupled theory overpredicts control authority during the first cycle. Note that from the results shown in Fig. 3, the deflection using the uncoupled model due to external piezoelectric actuation is larger compared to the T–P–M model under the same actuation. This implies that if piezoelectric force is used to control deflection, the uncoupled theory overestimates control authority. After the first cycle, this trend continues with a gain value of 50 as shown in Fig. 15. However, the trend is reversed (Fig. 16), that is, the coupled T–P–M model overestimates the control authority after the first cycle with a gain value of 100. This can be explained as follows. Because rate feedback is used, the piezoelectric force on the structure takes the form of structural damping, instead of a force vector. Contrary to the case studied in Fig. 3, piezoelectric control force does not influence equilibrium position, but rather vibration decay. Control authority is determined by the electrical signal received by actuators and the mechanical force due to the signal. For the two cases with different gain values, during the first cycle, the uncoupled theory produces smaller displacement because it has a greater ability to correct deflection with a certain piezoelectric actuation. However, this also implies that the actuators receive smaller electrical signals due to smaller displacement in the uncoupled model, which weakens its control ability. The result of combining these two opposite effects is determined by gain value. For the uncoupled model, if gain value is small, the effect of strengthening control authority is dominant and the uncoupled theory overestimates control authority. If gain value is large, the effect of weakening control authority is dominant and the uncoupled theory underestimates control authority. Figure 17 presents the ratio of equivalent modal structural damping due to control between the

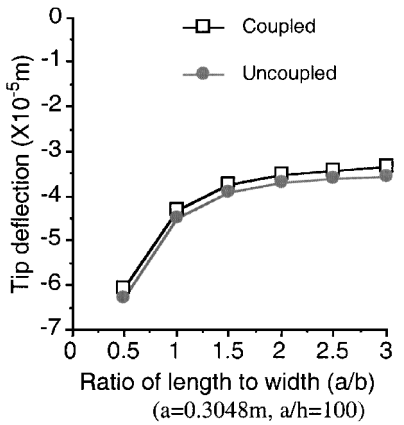

Fig. 14 Variation in tip deflections with length-to-width ratio a/b: surface heat flux $q_t = 3000$ W/m^2.

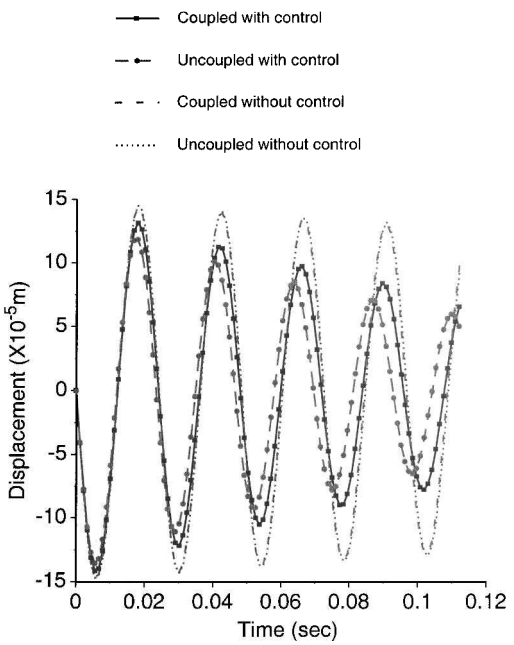

Fig. 15 Dynamic tip responses with control: $G = 50$, $a/h = 100$.

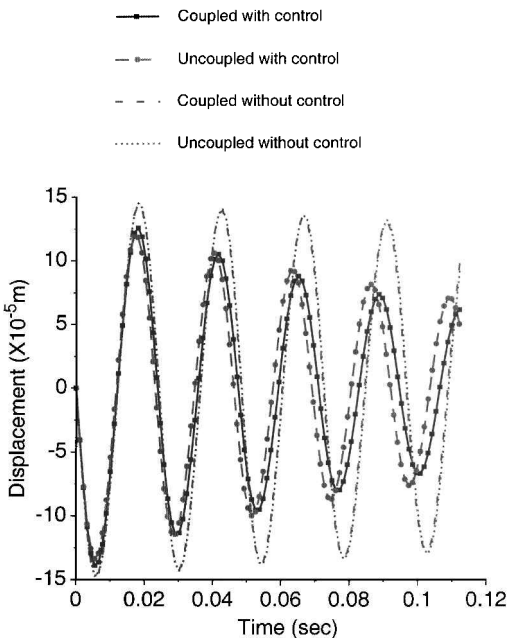

Fig. 16 Dynamic tip responses with control: $G = 100$, $a/h = 100$.

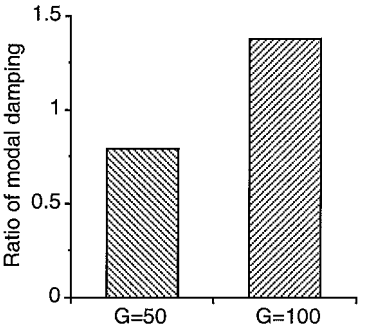

Fig. 17 Comparison of modal damping ratio with control, T–P–M model to uncoupled model: $a/h = 100$.

T–P–M model and the uncoupled model. For gain values of 50 and 100, the damping in the T–P–M model is 0.786 and 1.378 times that obtained using the uncoupled model, respectively. Therefore, the uncoupled theory overestimates control authority for small gain value and underestimates control authority for large gain value.

Conclusions

A completely coupled T–P–M theory, based on the higher-order displacement field and the higher-order temperature field, is developed to study dynamic responses of smart composite plates. The theory is implemented using a finite element technique that ensures the application of practical geometry and boundary conditions. Numerical results are presented for a cantilever composite plate with piezoelectric actuators. The plate is subjected to thermal, piezoelectric, and mechanical loads. The impact of various coupling effects is investigated in detail. The following important observations are made from this study:

1) The developed approach provides a means to accurately model the dynamic behavior of composite plates with piezoelectric actuators.

2) In open-loop conditions, coupling effects decrease both steady-state deflection and vibration amplitude due to the interaction between thermal, piezoelectric, and mechanical fields.

3) In closed-loop control, the uncoupled model, which neglects the coupling effects, overestimates control authority with a low gain value and underestimates control authority with a high gain value.

4) For surface-bonded actuators, the differences between the two theories are affected by the geometry of the actuators and the host structure. A critical parameter is the thickness ratio of actuator to plate. An increase in this ratio leads to rapid growth in the deviation between the two theories.

Appendix A: Functions in Higher-Order Temperature Assumption

The functions in Eq. (18) are defined as follows:

$$f(z) = z^2(a_1 + a_2 z) \tag{A1}$$

$$p_1(z) = 1 + b_1 z^2 + b_2 z^3 \tag{A2}$$

$$p_2(z) = z\left(1 + c_1 z + c_2 z^2\right) \tag{A3}$$

where

$$a_1 = \left\{\left[-\alpha_b \frac{h_v}{\kappa_{33}}(T_0 - T_\infty) + (1-\alpha_b)\frac{q_b}{\kappa_{33}}\right]A_{12} - \left[\alpha_t \frac{h_v}{\kappa_{33}}(T_0 - T_\infty) + (1-\alpha_b)\frac{q_s}{\kappa_{33}}\right]A_{22}\right\} \Big/ (A_{11}A_{22} + A_{12}A_{21}) \tag{A4}$$

$$a_2 = \left\{\left[\alpha_b \frac{h_v}{\kappa_{33}}(T_0 - T_\infty) - (1-\alpha_b)\frac{q_b}{\kappa_{33}}\right]A_{11} - \left[\alpha_t \frac{h_v}{\kappa_{33}}(T_0 - T_\infty) + (1-\alpha_t)\frac{q_s}{\kappa_{33}}\right]A_{21}\right\} \Big/ (A_{11}A_{22} + A_{12}A_{21}) \tag{A5}$$

$$b_1 = -\frac{h_v}{\kappa_{33}} \frac{\alpha_t A_{22} + \alpha_b A_{12}}{A_{11}A_{22} + A_{12}A_{21}} \tag{A6}$$

$$b_2 = \frac{h_v}{\kappa_{33}} \frac{\alpha_b A_{11} - \alpha_t A_{21}}{A_{11}A_{22} + A_{12}A_{21}} \tag{A7}$$

$$c_1 = \left[\left(1 + \alpha_b \frac{h_v}{\kappa_{33}}\frac{H}{2}\right)A_{12} - \left(1 + \alpha_t \frac{h_v}{\kappa_{33}}\frac{H}{2}\right)A_{22}\right] \Big/ (A_{11}A_{22} + A_{12}A_{21}) \tag{A8}$$

$$c_2 = \left[\left(1 + \alpha_t \frac{h_v}{\kappa_{33}}\frac{H}{2}\right)A_{21} + \left(1 + \alpha_b \frac{h_v}{\kappa_{33}}\frac{H}{2}\right)A_{11}\right] \Big/ (A_{11}A_{22} + A_{12}A_{21}) \tag{A9}$$

$$A_{11} = \alpha_t (h_v/\kappa_{33})(H^2/4) + H \tag{A10}$$

$$A_{12} = \alpha_t (h_v/\kappa_{33})(H^3/8) + (3H^2/4) \tag{A11}$$

$$A_{21} = \alpha_b (h_v/\kappa_{33})(H^2/4) + H \tag{A12}$$

$$A_{22} = \alpha_b (h_v/\kappa_{33})(H^3/8) + (3H^2/4) \tag{A13}$$

Here, κ_{33} denotes the thermal conductivity through the thickness of the plate. If the top surface heat flux q_s is specified, $\alpha_t = 0$. If the bottom surface heat flux q_b is specified, $\alpha_b = 0$. The positive direction of heat fluxes q_s and q_b is defined as the positive direction of z axis. If no heat flux is specified on the top surface, $\alpha_t = 1$. If no heat flux is specified on the bottom surface, $\alpha_b = 1$.

Appendix B: Matrices and Vectors in Governing Equation

Element matrices in Eq. (43) are defined as follows:

$$\boldsymbol{M} = \int_V \boldsymbol{B}_m^T \rho \boldsymbol{B}_m \, \mathrm{d}V \tag{B1}$$

$$\boldsymbol{C}_{uu} = \int_V \boldsymbol{B}_m^T \gamma \boldsymbol{B}_m \, \mathrm{d}V \tag{B2}$$

$$\boldsymbol{K}_{uu} = \int_V \boldsymbol{B}_u^T \boldsymbol{Q} \boldsymbol{B}_u \, \mathrm{d}V \tag{B3}$$

$$\boldsymbol{K}_{u\phi} = -\int_V \boldsymbol{B}_u^T \boldsymbol{P} \boldsymbol{B}_\phi \, \mathrm{d}V \tag{B4}$$

$$\boldsymbol{K}_{u\theta} = -\int_V \boldsymbol{B}_u^T \boldsymbol{k} \boldsymbol{B}_\theta \, \mathrm{d}V \tag{B5}$$

$$\boldsymbol{K}_{\phi u} = \boldsymbol{K}_{u\phi}^T \tag{B6}$$

$$\boldsymbol{K}_{\phi\phi} = -\int_V \boldsymbol{B}_\phi^T \boldsymbol{B} \boldsymbol{B}_\phi \, \mathrm{d}V \tag{B7}$$

$$\boldsymbol{K}_{\phi\theta} = -\int_V \boldsymbol{B}_\phi^T \boldsymbol{d} \boldsymbol{B}_\theta \, \mathrm{d}V \tag{B8}$$

$$\boldsymbol{K}_{\theta\theta} = -\int_V \boldsymbol{B}_p^T \kappa \boldsymbol{B}_p \, \mathrm{d}V \tag{B9}$$

$$\boldsymbol{C}_{\theta u} = T_0 \boldsymbol{K}_{u\theta}^T \tag{B10}$$

$$\boldsymbol{C}_{\theta\phi} = T_0 \boldsymbol{K}_{\phi\theta}^T \tag{B11}$$

$$\boldsymbol{C}_{\theta\theta} = -T_0 \int_V \boldsymbol{B}_\theta^T a_T \boldsymbol{B}_\theta \, \mathrm{d}V \tag{B12}$$

$$\boldsymbol{F}_u = \int_S \boldsymbol{B}_m^T \boldsymbol{t} \, \mathrm{d}S \tag{B13}$$

$$\boldsymbol{F}_\phi = \int_S \boldsymbol{B}_n^T q_e \, \mathrm{d}S \tag{B14}$$

$$\boldsymbol{F}_\theta = \int_S \boldsymbol{B}_\theta^T q_t \, \mathrm{d}S \tag{B15}$$

$$\boldsymbol{F}_{u\theta} = \int_V \boldsymbol{B}_u^T \boldsymbol{k} f(z) \, \mathrm{d}V \tag{B16}$$

$$\boldsymbol{F}_{\phi\theta} = \int_V \boldsymbol{B}_\phi^T \boldsymbol{d} f(z) \, \mathrm{d}V \tag{B17}$$

$$\boldsymbol{F}_{\theta\theta} = \int_V \boldsymbol{B}_p^T \kappa \boldsymbol{L} f(z)\, \mathrm{d}V \tag{B18}$$

where

$$\boldsymbol{L} = \left[\frac{\partial}{\partial x} \quad \frac{\partial}{\partial y} \quad \frac{\partial}{\partial z} \right]^T$$

Acknowledgments

The research is supported by NASA Langley Research Center, Grant NAG-1-1988, Technical Monitor Carol D. Wieseman.

References

[1]Crawley, E. F., and de Luis, J., "Use of Piezoelectric Actuators as Elements of Intelligent Structures," *AIAA Journal*, Vol. 25, No. 10, 1987, pp. 1373–1385.

[2]Lee, C. K., "Theory of Laminated Piezoelectric Plates for the Design of Distributed Sensors/Actuators. Part I: Governing Equations and Reciprocal Relationships," *Journal of the Acoustical Society of America*, Vol. 87, No. 3, 1990, pp. 1144–1158.

[3]Mitchell, J. A., and Reddy, J. N., "A Refined Hybrid Plate Theory for Composite Laminates with Piezoelectric Laminae," *International Journal of Solids Structure*, Vol. 32, No. 16, 1995, pp. 2345–2367.

[4]Chattopadhyay, A., and Gu, H., "New Higher-Order Plate Theory in Modeling Delamination Buckling of Composite Laminates," *AIAA Journal*, Vol. 32, No. 8, 1994, pp. 1709–1716.

[5]Mindlin, R. D., "Equations of High Frequency Vibrations of Thermopiezoelectric Crystal Plates," *International Journal of Solids Structure*, Vol. 10, No. 5, 1974, pp. 625–632.

[6]Mukherjee, N., and Sinha, P. K., "A Finite Element Analysis of Thermostructural Behavior of Composite Plates," *Journal of Reinforced Plastics and Composites*, Vol. 12, No. 11, 1993, pp. 1026–1042.

[7]Tauchert, T. R., "Piezothermoelastic Behavior of a Laminated Plate," *Journal of Thermal Stresses*, Vol. 15, No. 1, 1992, pp. 25–37.

[8]Lee, H., and Saravanos, D. A., "Effect of Temperature-Induced Material Property Variations on Piezoelectric Composite Plates," *Proceedings of the AIAA/ASME/ASCE/AHS/ASC 37th Structures, Structural Dynamics and Materials Conference*, AIAA, Reston, VA, 1996, pp. 1781–1788.

[9]Lee, H., and Saravanos, D. A., "Active Compensation of Thermally Induced Bending and Twisting in Piezoceramic Composite Plates," *Proceedings of the AIAA/ASME/ASCE/AHS/ASC 38th Structures, Structural Dynamics and Materials Conference*, AIAA, Reston, VA, 1997, pp. 120–130.

[10]Chattopadhyay, A., Li, J., and Gu, H., "Coupled Thermo-Piezoelectric-Mechanical Model for Smart Composite Laminates," *AIAA Journal*, Vol. 37, No. 12, 1999, pp. 1633–1638.

[11]Gu, H., Chattopadhyay, A., Li, J., and Zhou, X., "A Higher Order Temperature Theory for Coupled Thermo-Piezoelectric-Mechanical Modeling of Smart Composites," *International Journal of Solids and Structures* (to be published).

A. M. Baz
Associate Editor